Calculation and Modeling of EMI from Integrated Circuits inside High-Speed Network Devices

Sotirios K. GOUDOS

Telecommunications Center, Aristotle University of Thessaloniki, Thessaloniki 54124, Greece,

sgoudo@physics.auth.gr

Abstract. *This work presents a numerical approach to the modeling of Electromagnetic Interference (EMI) from the emissions of ICs and PCBs inside rectangular metallic enclosures of network devices. The ICs are modeled as small magnetic and electric dipoles. Their interaction with the enclosures is studied with the dyadic Green's functions. Several calculation examples of surface current density on the metallic walls are given due to dipoles parallel to all directions. A Probabilistic Model is created from magnetic probe measurements in various types of router devices. Monte Carlo simulation is applied in order to perform a worst-case analysis. The applications of the above approach in PCB design are discussed.*

Keywords

Numerical techniques, Electromagnetic interference, Printed circuit board design, Monte Carlo simulation.

1. Introduction

Electromagnetic interference (EMI) inside metallic enclosures is a critical issue during the design stage of Printed Circuit Boards (PCBs). It is very important for the EMC engineer to be able to perform a worst-case analysis of the EMI on the enclosure metallic walls. The placement of Integrated Circuits (ICs) on PCBs inside a shielded enclosure has an effect on the interference issue. Integrated circuits can be modeled in the form of small magnetic or electric dipoles. The validity of this modeling has been verified after suitable characterizations and measurements of several types of telecommunications equipment.

Cooray et al. [1] modeled ICs as small electric and magnetic current sources and used the dyadic Green's functions for field calculation. The method for measuring electric and magnetic dipole moments from ICs is described by Goulette in [2]. The interaction between cavity walls and internal dipoles can be described by using the dyadic Green's functions [3]. The mapping matrix approach is subsequently applied [4]-[6]. This approach outlines the interaction between the metallic walls inside the enclosure and the dipoles. In the present work, the electric

surface current density induced on metallic walls of a rectangular cavity due to magnetic and electric dipole is computed.

It is noticed that the accurate prediction of electromagnetic emissions from PCBs is difficult or almost impossible. Due to the above, a stochastic procedure is proposed. Routers are the most common high-speed network devices in modern networks. A probabilistic model of modern router devices will be given, which is based on magnetic probe measurements. Monte Carlo simulation is applied using both source existence and source amplitude probabilistic distributions in order to perform a worst-case analysis.

This paper is organized as follows: Section 2 presents the formulation with closed form expressions. Section 3 describes the high-speed network equipment model created based on measurement data and gives electric current density calculation examples. In Section 4 the Monte Carlo simulation details can be found. Finally the conclusions are given in Section 5.

2. Formulation

For a rectangular cavity with dimensions *a*, *b* and *c*, ($a=c=L$, $b=0.3L$), along *x*, *y* and *z*-axis respectively (see Fig. 1), the expressions for dyadic Green's function of the electric and the magnetic vector potential are given in [4]-[5]. The enclosure walls are assumed to be Perfect Electric Conductors (PEC).

For a small electric and a small magnetic dipole source placed at $\bar{r}'$ inside the cavity the current densities are given:

$$\bar{J}_e(\bar{r}') = (p_x\hat{x} + p_y\hat{y} + p_z\hat{z})\delta(\bar{r} - \bar{r}'), \qquad (1)$$

$$\bar{J}_m(\bar{r}') = (m_x\hat{x} + m_y\hat{y} + m_z\hat{z})\delta(\bar{r} - \bar{r}') \qquad (2)$$

where $\bar{r}$ and $\bar{r}'$ are the vector positions of the field and the source point, p_x, p_y, p_z are the components of the electric dipole moments, and m_x, m_y, m_z the corresponding magnetic dipole moments in the $\hat{x}, \hat{y}$ and $\hat{z}$ directions respectively. The electric and magnetic field induced inside

the cavity by the small electric dipole with current density $\overline{J}_e(\overline{r}')$ are given by:

$$\overline{E}^e(\overline{r}) = \int_{V'} \overline{\overline{G}}_e(\overline{r}\,|\,\overline{r}')\square \overline{J}_e(\overline{r}')dV',\tag{3}$$

$$\overline{H}^e(\overline{r}) = \frac{1}{j\omega\mu_o}\int_{V'}\overline{\overline{G}}_h(\overline{r}\,|\,\overline{r}')\square \overline{J}_e(\overline{r}')dV'\tag{4}$$

where $\overline{r}$ and $\overline{r}'$ are the vector positions of the field and the source point, V' is the source volume over which the current density is distributed, $\overline{\overline{G}}_e$ and $\overline{\overline{G}}_h$ are the dyadic Green's functions for the E and H fields due to an electric dipole source inside a rectangular cavity. Similarly the fields due to a magnetic current density $\overline{J}_m(\overline{r}')$ are:

$$\overline{E}\ (\overline{r}) = -\frac{1}{j\omega\mu_o}\int_{V'}\overline{\overline{g}}_e(\overline{r}\,|\,\overline{r}')\square \overline{J}_m(\overline{r}')dV',\tag{5}$$

$$\overline{H}\ (\overline{r}) = \int_{V'}\overline{\overline{g}}_h(\overline{r}\,|\,\overline{r}')\square \overline{J}_m(\overline{r}')dV'\tag{6}$$

where $\overline{r}$ and $\overline{r}'$ are the vector positions of the field and the source point, V' is the source volume over which the current density is distributed, $\overline{\overline{g}}_e$ and $\overline{\overline{g}}_h$ the dyadic Green's functions for the E and H fields, respectively, due to a magnetic dipole source. The closed form expressions for the induced surface current density on the $z=c$ wall (for $z>z'$) due to the electric dipole moments p_x, p_y, p_z and the magnetic dipole moments m_x, m_y, m_z are given by:

$$\overline{J}_S = \frac{p_x}{j\omega\mu_0 ab}\sum_m\sum_n e_m e_n\left(\frac{\sin(k_g z')}{\sin(k_g c)}\right)\times\tag{7}$$
$$\cos(k_x x)\sin(k_y y)\cos(k_x x')\sin(k_y y')\hat{x}$$

$$\overline{J}_S = \frac{-p_y}{j\omega\mu_0 ab}\sum_m\sum_n e_m e_n\left(\frac{\sin(k_g z')}{\sin(k_g c)}\right)\times\tag{8}$$
$$\sin(k_x x)\cos(k_y y)\sin(k_x x')\cos(k_y y')\hat{y}$$

$$\overline{J}_S = \frac{p_z}{j\omega\mu_0 ab}\sum_m\sum_n e_m e_n\left(\frac{\cos(k_g z')}{k_g\sin(k_g c)}\right)\times\tag{9}$$
$$[k_x\cos(k_x x)\sin(k_y y)\sin(k_x x')\sin(k_y y')\hat{x}+$$
$$k_y\sin(k_x x)\cos(k_y y)\sin(k_x x')\sin(k_y y')\hat{y}]$$

$$\overline{J}_s = \frac{m_x}{ab}\sum_m\sum_n e_m e_n\left[\frac{1}{k_g k_c^{\,2}}\left(\frac{\cos(k_g z')}{\sin(k_g c)}\right)\right]\times\tag{10}$$
$$\left\{-k_x k_y\begin{bmatrix}\sin(k_x x)\cos(k_y y)\cos(k_x x')\sin(k_y y')+\\ \dfrac{k_g^2}{k^2}\cos(k_x x)\sin(k_y y)\sin(k_x x')\cos(k_y y')\end{bmatrix}\hat{x}\right.$$
$$\left.+k_x^2\begin{bmatrix}\cos(k_x x)\sin(k_y y)\cos(k_x x')\sin(k_y y')+\\ \dfrac{k_g^2}{k^2}\sin(k_x x)\cos(k_y y)\sin(k_x x')\cos(k_y y')\end{bmatrix}\hat{y}\right\}$$

$$\overline{J}_s = \frac{-m_y}{ab}\sum_m\sum_n e_m e_n\left[\frac{1}{k_g k_c^{\,2}}\left(\frac{\cos(k_g z')}{\sin(k_g c)}\right)\right]\times\tag{11}$$
$$\left\{k_y^2\begin{bmatrix}\cos(k_x x)\sin(k_y y)\cos(k_x x')\sin(k_y y')+\\ \dfrac{k_g^2}{k^2}\cos(k_x x)\sin(k_y y)\cos(k_x x')\sin(k_y y')\end{bmatrix}\hat{x}\right.$$
$$\left.+k_x k_y\begin{bmatrix}\cos(k_x x)\sin(k_y y)\sin(k_x x')\cos(k_y y')+\\ \dfrac{k_g^2}{k^2}\sin(k_x x)\cos(k_y y)\cos(k_x x')\sin(k_y y')\end{bmatrix}\hat{y}\right\}$$

$$\overline{J}_s = \frac{m_z}{ab}\sum_m\sum_n e_m e_n\left[\frac{1}{k^2}\left(\frac{\sin(k_g z')}{\sin(k_g c)}\right)\right]\times\tag{12}$$
$$\left\{-k_y\left[\cos(k_x x)\sin(k_y y)\cos(k_x x')\cos(k_y y')\right]\hat{x}\right.$$
$$\left.+k_x\left[\sin(k_x x)\cos(k_y y)\cos(k_x x')\cos(k_y y')\right]\hat{y}\right\}$$

The coefficients in (7)-(12) are given below:

$$k = \omega\sqrt{\mu_0\varepsilon_0} = \frac{2\pi}{\lambda},\ k_x = \frac{m\pi}{a},\ k_y = \frac{n\pi}{b},\ k_z = \frac{l\pi}{c},\tag{13}$$
$$k_c^2 = k_x^2 + k_y^2,\ k_g^2 = (k^2 - k_c^2),\ e_i = \begin{cases}1 & i=0\\2 & i\neq 0\end{cases}$$
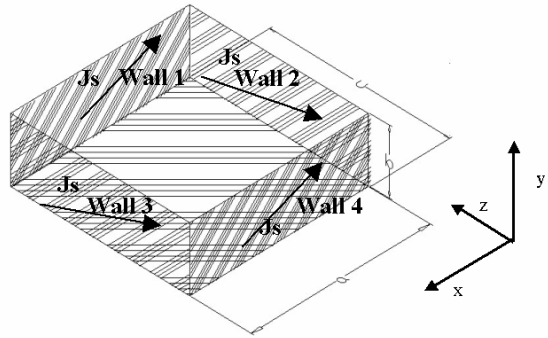
Fig. 1. Rectangular enclosure geometry.

It is interesting to notice that if in expressions (7), (9) and (11) we use $y'=0$ then the currents induced due to electric dipoles parallel to x and z axis and the x-component of the current due to magnetic dipole parallel to y axis vanish. It is evident from equations (7) - (12) that the surface current density depends on the cavity geometry, the source frequency (or wavelength) and the source dipole moment. Normalization of (4) in terms of wavelength allows for a wider interpretation of the results. For example (12) becomes:

$$\overline{J}_s\lambda = \frac{m_z}{\alpha\beta}\sum_m\sum_n e_m e_n\left[\frac{1}{\kappa^2}\left(\frac{\sin(k_g z')}{\sin(k_g c)}\right)\right]\times\tag{14}$$
$$\left\{-\kappa_y\left[\cos(k_x x)\sin(k_y y)\cos(k_x x')\cos(k_y y')\right]\hat{x}+\right.$$
$$\left.+\kappa_x\left[\sin(k_x x)\cos(k_y y)\cos(k_x x')\cos(k_y y')\right]\hat{y}\right\}$$

where

$$a = \alpha\lambda, b = \beta\lambda, \kappa_x = \frac{m\pi}{\alpha}, \kappa_y = \frac{n\pi}{\beta},$$

$$\kappa = 2\pi, \kappa_g = \sqrt{\kappa_x^2 + \kappa_y^2 - 4\pi^2}$$

(15)

In all numerical results in the following sections the normalized expressions have been used.

3. Router Device Model

Various types of network equipment can include multiple source systems within rectangular shielded enclosures. Multiple sources inside the rectangular cavity of Fig.1 are assumed. If N possible cavity sources exist and M wall points of interest are taken into account then the amplitude mapping of every source to a specific point on the wall can be represented by an $N \times M$ matrix $\mathbf{A}$ [4]-[6], called mapping matrix. In $\mathbf{A}$, a matrix element ρ_{ij} represents the disturbance on j^{th}-point caused by the ith-source. Disturbances caused by multiple sources at the same reference wall point can be summed using the principle of superposition.

The deterministic values calculated in the mapping matrix are accurate enough only if all the source characteristics (magnitude, polarization and phase) are modeled correctly. The accurate prediction of electromagnetic emission from multiple source systems is a difficult or even impossible task due to their complexities. A stochastic approach like Monte Carlo simulation can be applied. Such an approach has the advantage of proving a quantification of major trends in multiple source systems.

3.1 Magnetic Probe Measurements

In order to have more accurate results for the Monte Carlo simulation there is the need to create a generic probabilistic model of a router device based on measurement data. The emission levels of various ICs inside different routers have been measured. Source existence and source magnitude probability distributions have been created for the most important operating frequencies based solely on measurements.

The measurements were performed using the appropriate probes Chase MFP9150 (9 kHz–30 MHz) and Chase MFP9151 (30 MHz–1 GHz). The probes were connected to a Spectrum Analyzer (EMI Receiver) at the peak detection mode. Probes are oriented in space in order to have the maximum coupling with the magnetic field. By applying the antenna factors of the probes it is possible to obtain the near magnetic field in dB (μA/m) at the probe tip.

To relate the magnetic field measurement to a magnetic dipole moment it is necessary to consider the radiating areas of the corresponding currents loops. By performing measurements in two different distances from the loop the magnetic moment can be calculated [1]. It is noticed that the measured field components are very sensitive

to the probe location. To measure a magnetic field around a current loop or a field with high gradient flux lines the EMC engineer must observe the field in two normal orientations at the probe tip and finally select the proper orientation of the probe. It is important to notice that before the measurements the operational characteristics of the probe must be checked.

Various types of router devices, that are commonly used, were measured. These operate at high data speeds like Fast Ethernet (100 Mbps) or Gigabit Ethernet (1 Gbps). Common emission frequencies for such devices are relatively low below 100 MHz. This is due to fact that the CPU speed requirements for such equipment are not as high as for modern PCs.

3.2 Model Description

Router devices can be found in every modern network. A typical router photo is given in Fig. 2. Modern routers work at high data speeds (100 Mbps or higher). A router device has ICs placed not in symmetrical positions but in general in distinct areas of the PCB. Based on the measurements taken for different router models three distinct areas can be found in a common router: the RAM area where all the router SDRAM ICs are placed, the CPU area at the middle of the board and the area where the Fast Ethernet transceiver is placed. It must be noticed that all modern routers have Fast Ethernet interfaces for both networking and management purposes.
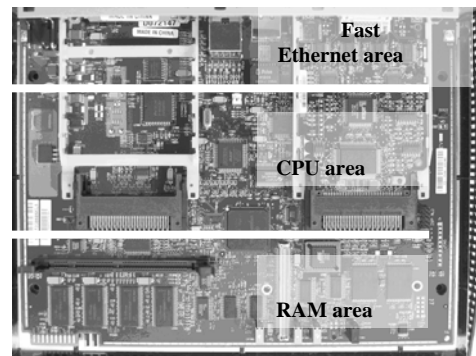
Fig. 2. A typical router.

A generic simplified model of a router PCB was created (Fig. 3).
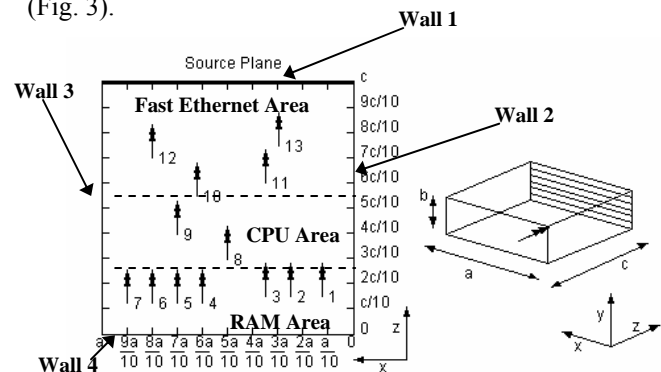
Fig. 3. Simplified router model.

For $L=0.045\lambda$ it has been found that the most probable maximum number of sources is 13. They are all placed in asymmetrical positions. This type of model has been found to be independent of router specific interface cards. The source existence and amplitude probability distributions for this router model were found. The different router areas have different source existence probabilities. These are given in Tab. 1. The amplitude distributions found are in Tab. 2.

Area	Maximum source number	Source existence p
RAM	7	1.0
CPU	2	0.7
Fast Ethernet	4	0.5

Tab. 1. Source existence probabilistic distributions for the Router model.

	Magnitude order	p
$L = 0.045\ \lambda$	1	0.1
	5×10^{-2}	0.6
	2×10^{-1}	0.3

Tab. 2. Magnetic dipole moment magnitude probabilistic model for the Router model.

3.3 Numerical Results

In all results that follow the sources are assumed to be placed at the bottom of the cavity at $y'=0$ for $L=0.045\lambda$. The electric surface current density due to the sum of all sources is calculated on 256 x 160 wall points. A plot of the surface current density due to 13 magnetic dipoles parallel to x-axis is given in Fig. 4a and Fig 4b for x and y current component respectively.

One may notice that the x-component represents an anti-symmetric behavior while the y current component shows a symmetric one. The current values due to y-component are an order of a magnitude higher than those of the x-component. The similar plot of the surface current density due to 13 magnetic dipoles parallel to z-axis is given in Figs. 5a,b.
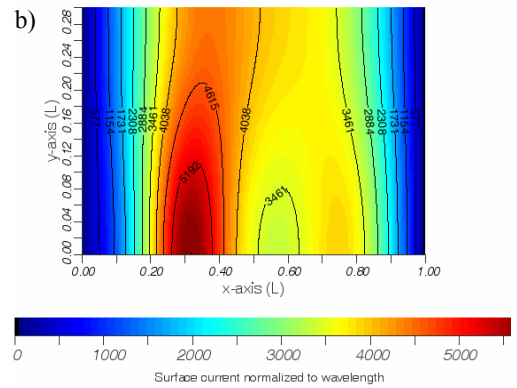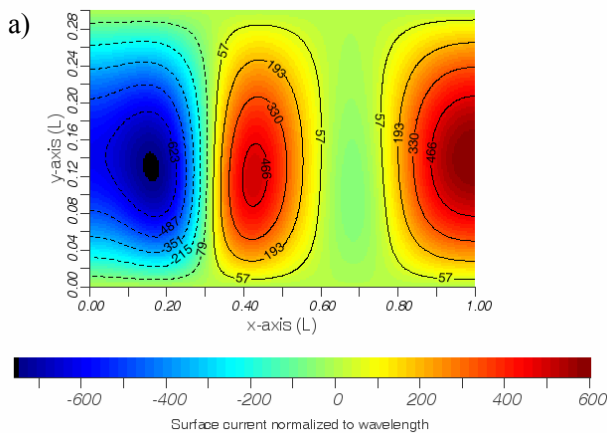
Fig. 4. Contour plot of wall surface current due to 13 magnetic dipoles parallel to x-axis on Wall 1 for $L = 0.045\ \lambda$ a) x-component b) y-component.
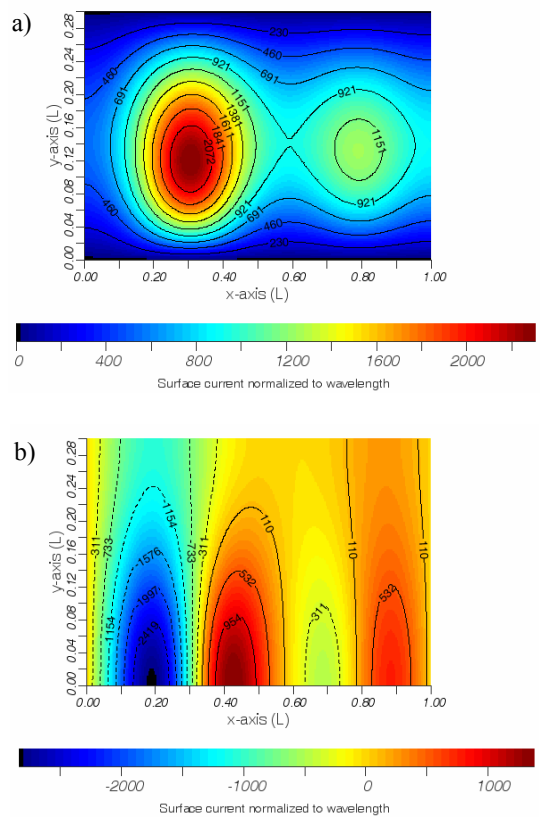
Fig. 5. Contour plot of wall surface current due to 13 magnetic dipoles parallel to z-axis on Wall 1 for $L = 0.045\ \lambda$ a) x-component b) y-component.

The surface current density due to electric dipoles parallel to y-axis is depicted in Fig. 6. This current density is about two orders of a magnitude less than the one due to magnetic dipoles. It is therefore clear that the dominant contribution to wall currents is due to magnetic dipoles.

The anti-symmetric behavior is obvious for Figs. 4a and 5b while the symmetric one is shown in Figs. 4b, 5a and 6. Especially the y-current component coming from the magnetic dipoles parallel to z-axis presents particular interest since it is anti-symmetric and it has the highest values (among anti-symmetric components). Due to the

fact that the higher induced current values are from magnetic dipoles only that type of sources will be used in the results to follow. Random source configurations may produce different results, as it will be shown below. The surface current density y-component due to 13 magnetic dipoles parallel to z-axis for wall 4 is shown in Fig 7.
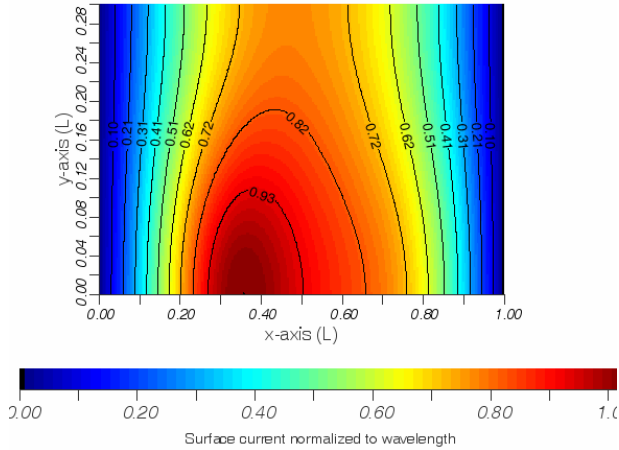
Fig. 6. Contour plot of wall surface current due to 13 electric dipoles parallel to y-axis on Wall 1 for $L = 0.045 \lambda$.
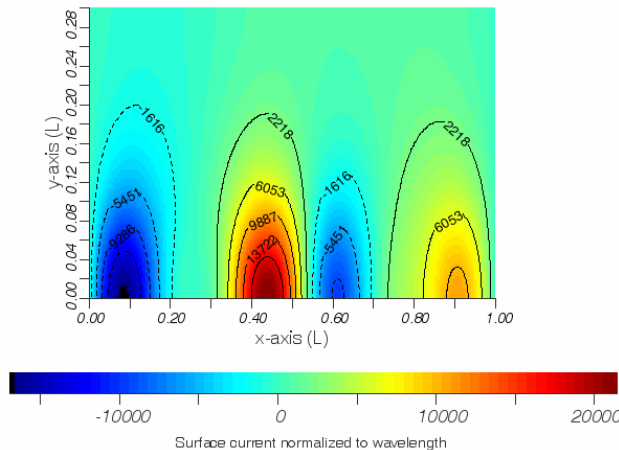
Fig. 7. Contour plot of wall surface current y-component due to 13 magnetic dipoles parallel to z-axis on Wall 4 for $L = 0.045 \lambda$.

The current values on wall 4 are an order of a magnitude higher than those on wall 1. Such a difference can be explained by the fact that the sources are placed closer to wall 4 than to wall 1 and their number is larger than those close to wall 1. The larger values on wall 1 are at the bottom left part. This is due to the fact that more sources are placed near the left part of the PCB and therefore contributing to the left part of the wall. The induced current density on wall 4 has the higher values near the wall bottom.

4. Monte Carlo Simulation

Monte Carlo simulation is a powerful tool that has been applied successfully in many different engineering problems [7]. Monte Carlo simulations that are based on

probability distributions describing source existence and amplitude levels can give a first approximation of the emission level margins and perform a worst-case analysis.

Monte Carlo simulations based on probability distributions describing source existence and amplitude levels were performed for the router model described above. The whole procedure is described below:

Step 1: Mapping Matrix Calculation. The mapping matrices are evaluated using the closed form expressions given in section 2.

Step 2 Loop process: A loop is performed with an adequate number of iterations. During the loop process a random set of sources is generated according to a known probabilistic distribution [8]. All the elements ρ_{ij} of the mapping matrix are multiplied by a Bernoulli random variable, ζ_i that lies in the set of values [0,1]. The existence of source i is modeled using this Bernoulli random variable. The result is a new matrix $\mathbf{A}'$ given by [5]:

$$\mathbf{A}' = \begin{bmatrix} \rho_{11}\zeta_1 & \cdots\cdots\cdots\cdots\cdots\rho_{1(m-1)}\zeta_1 & \rho_{1m}\zeta_1 \\ \rho_{21}\zeta_2 & \cdots\cdots\cdots\cdots\cdots\rho_{2(m-1)}\zeta_2 & \rho_{2m}\zeta_2 \\ . & & \\ . & & \\ . & & \\ \rho_{n1}\zeta_n & \cdots\cdots\cdots\cdots\cdots\rho_{n(m-1)}\zeta_n & \rho_{nm}\zeta_n \end{bmatrix} \quad (16)$$

Amplitude distributions can be also applied. In such a case different amplitude levels $a_1, a_2, \ldots, a_n$ are assigned with probabilities $p_1 p_2, \ldots, p_n$. The amplitude distribution is multiplied with the source existence one. Therefore the random variable ζ_i is then given by:

$$\zeta_i = \zeta_{ie}\zeta_{ia} \quad (17)$$

where ζ_{ie} the random variable of the source existence distribution and ζ_{ia} the random variable of the amplitude distribution. Matrix $\mathbf{A}'$ is calculated for every iteration.

Step 3: Statistical processing of the results. After the end of the Monte Carlo simulation the statistical processing begins. The wall points of the probable larger current density values are found. The statistical analysis of the results involves calculation of the 90th percentile, mean and standard deviation values. The 90th percentile gives the value below of which lie the 90% of the samples.

Monte Carlo simulation using both source existence and amplitude distribution was applied on the router model presented in the previous section. The electric current density is found for 15 wall points inside the cavity. The positions of these wall points are given in Fig. 8.
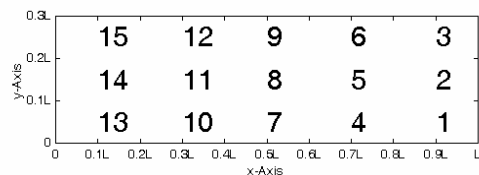
Fig. 8. Wall points of interest.

After each simulation the statistical results mean, standard deviation, 90th percentile are compared with the sum of all sources on every wall point. The results are presented below.

Monte Carlo simulation was applied for both opposite walls 1 and 4 (Fig. 1) with both amplitude and source existence probability distributions. Figs. 9a-9b have the Monte Carlo simulation results for the electric surface current density y component due to *z* directed magnetic dipoles.

a)

Js (Normalized)

■ Mean □ Standard Deviation □ 90th Percentile ▨ Sum of sources

b)

Js (Normalized)

■ Mean □ Standard Deviation □ 90th Percentile ▨ Sum of sources
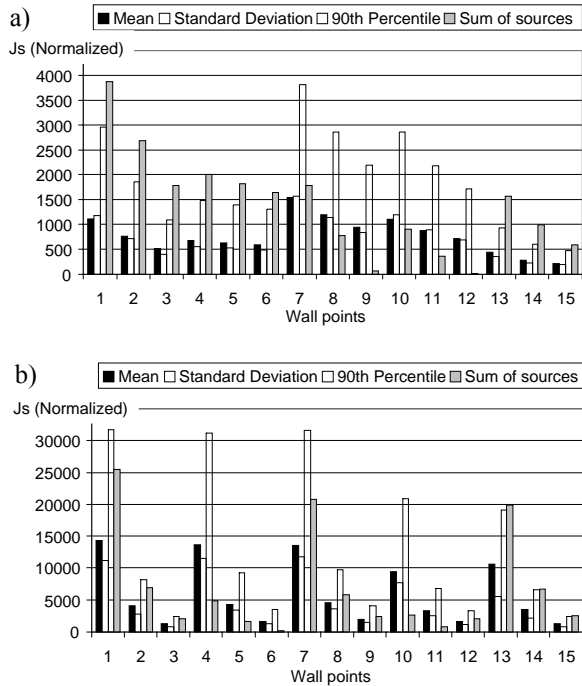
Fig. 9. The y-component of induced current on wall points due to magnetic dipoles parallel to z axis with non-equal magnetic moments after Monte Carlo simulation. The results are for the router equipment model for (a) Wall 1and (b) Wall 4.

One may notice that the current density is much higher in wall 4, due to the fact that more sources are closer to wall 4 than to wall 1. For wall 1 and 4 the higher current values are at wall points 1, 4, 7 at the bottom of the enclosure wall. For wall 1 the middle points 7, 8, 9 have all high current values. It is observed that there are wall points in both walls where the 90th percentile values are much higher than the sum of all sources.

The Monte Carlo simulation results, for the surface current density y component due to magnetic dipoles parallel to x-axis, are shown in Figs. 10a-10b. An interesting observation is that the results now show higher values than the previous ones. For wall 1 the sum of all sources is larger than the 90th percentile values. The higher values are in the middle of the wall (4, 5, 6, 7, 8, 9, 10, 11, and 12). In wall 4 the higher values are at the bottom wall points (1, 4, 7, 10, and 13). As in Fig 9 the 90th percentile values at these wall points are higher than the sum of all sources.

Another point worth noticing for all simulation results is the fact that in some points the standard deviation values are higher than the mean indicating a large dispersion of current values.

a)

Js (Normalized)

■ Mean □ Standard Deviation □ 90th Percentile ▨ Sum of sources

b)

Js (Normalized)

■ Mean □ Standard Deviation □ 90th Percentile ▨ Sum of sources
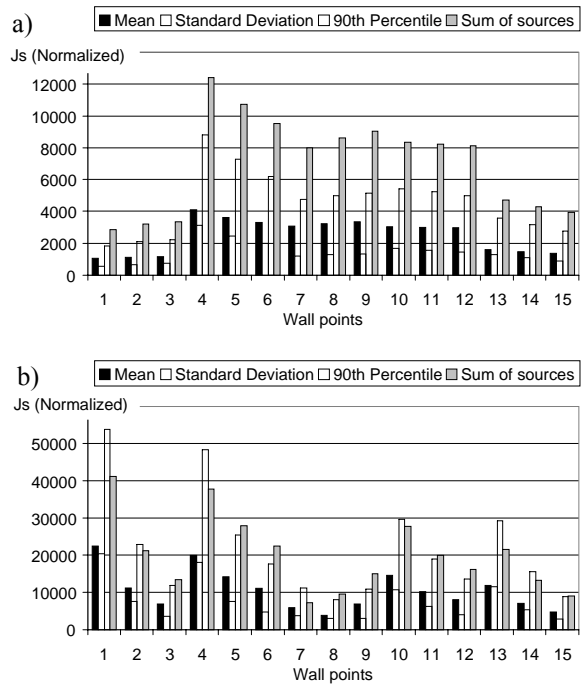
Fig. 10. The y-component of induced current on wall points due to magnetic dipoles parallel to x axis with non-equal magnetic moments after Monte Carlo simulation. The results are for the router equipment model for (a) Wall 1and (b) Wall 4.

5. Conclusion

In this work, numerical techniques are combined with stochastic procedures, in order to model EMI inside metallic enclosures of router devices. The generic router model presented is based on magnetic probe measurements of emission levels from ICs inside various devices. This router model has its sources placed in asymmetrical positions in three distinct areas on the PCB. The magnetic dipole sources placed in the PCB plane induce the higher current values in enclosure walls. The electric and magnetic dipole sources normal to the PCB plane induce at least two orders of a magnitude less current values. In order to perform a worst-case analysis Monte Carlo simulation can be applied. Simulation results have shown that due to asymmetrical behavior of the y current component due to magnetic dipoles parallel to z-axis the 90th percentile presents in some cases higher values than the sum of all sources. Therefore Monte Carlo simulation can be a useful tool in predicting emission level margins. Similar methods can be applied to a variety of equipment. Network equipment manufacturers can easily apply these techniques in order to make early risk limiting decisions during PCB design process.

Acknowledgements

References

[1] COORAY, F. R., CRAWHALL, R., COSTACHE, G. I. Radiated fields from circuit components inside rectangular enclosures with apertures. *Canadian Journal of Electrical and Computer Engineering.* 1991, vol. 16, no. 4, p. 143-147.

[2] GOULETTE, R. R. The measurement of radiated emissions form integrated circuits. In *Proceedings of the IEEE International EMC Symposium.* Anaheim, (USA), 1992, p.340-345.

[3] TAI, C. T., ROZENFELD, P. Different representations of dyadic Green's functions for a rectangular cavity. *IEEE Transactions on Microwave Theory and Techniques.* 1976, vol. 24, no. 9, p. 597-601.

[4] CRAWHALL, R. *EMI Potential of Multiple Sources within a Shielded Enclosure.* Doctoral Thesis, University of Ottawa, Ottawa, 1993.

[5] GOUDOS, S. K., VAFIADIS, E., SAHALOS, J. N. Monte Carlo simulation for the prediction of the emission level from multiple sources inside shielded enclosures. *IEEE Transactions on Electromagnetic Compatibility.* 2002, vol. 44, no. 2, p. 291-308.

[6] GOUDOS S. K., SAMARAS, T., VAFIADIS E., SAHALOS, J. N. Numerical approaches for EMI reduction of ICs and PCBs inside metallic enclosures. In *Proceedings of the IEEE International Symposium on Electromagnetic Compatibility.* Istanbul (Turkey), 2003, p. 513-518.

[7] RUBINSTEIN, R. Y. *Simulation and the Monte Carlo method.* New York: John Wiley & Sons, 1981.

[8] PAPOULIS, A. *Probability, Random Variables and Stochastic Processes.* Second Edition. New York: McGraw-Hill Series in Electrical Engineering, 1984.

About Authors...

Sotirios K. GOUDOS was born in Thessaloniki, Greece on June 20, 1968. He received the B.Sc. degree in Physics in 1991 and the M.Sc. of Postgraduate Studies in Electronics in 1994 both from the Aristotle University of Thessaloniki. In 2001 he received his Ph.D. degree in Physics from the Aristotle University of Thessaloniki and in 2005 the Master in Information Systems from the University of Macedonia. Since 1996 he has been working in the administration of the Telecommunications network at the Aristotle University of Thessaloniki, Greece. Since 2004 he is a part-time lecturer in the Department of Technology Management, University of Macedonia, Greece. His research interests include antenna design, electromagnetic compatibility, evolutionary computation algorithms and mobile communications. Dr. Goudos is a member of IEEE, Greek Physics Society and Greek Computer Society.

Topics:

1. Solid State Devices;
   a. CAD/CAM of Solid State Devices;
2. Vacuum and Micro-vacuum SHF Devices;
3. Microwave Communications, Broadcasting and Navigation Systems;
4. Antennas and Antenna Elements;
5. Passive Components;
   a. Materials and Technology of Microwave Devices;
   b. Nano-electronics and Nano-technology;
6. Very High Power Microwave Electronics and Effects;
7. Microwave Measurements;

8. Microwave Applications;
   a. Medical and Ecological Applications
9. Radio-astronomy, Remote Sensing, and Waves Propagation;
10. Resistance to Radiation and Electromagnetic-Pulse Damages;
H. History of Microwave and Telecommunication Technology;
W. Training of Radio-engineers and Specialists in the Field of Telecommunications

Deadline:

May 11, 2007 (camera-ready papers)

www.crimico.org